Research Article | Vol. 25, No. 14 | 10 Jul 2017 | OPTICS EXPRESS 15699
Optics EXPRESS

Label-free quantitative 3D tomographic imaging for partially coherent light microscopy

JUAN M. SOTO, JOSÉ A. RODRIGO,* AND TATIANA ALIEVA

Universidad Complutense de Madrid, Facultad de Ciencias Físicas, Ciudad Universitaria s/n, Madrid 28040, Spain
*jarmar@fis.ucm.es

Abstract: Crucial benefits provided by partially coherent light microscopy such as improved spatial resolution, optical sectioning and speckle-noise suppression are exploited here to achieve 3D quantitative imaging: reconstruction of the object refractive index (RI). We present a partially coherent optical diffraction tomography technique (PC-ODT) that can be easily implemented in commercially available bright-field microscopes. We show that the high numerical apertures of the objective and condenser lenses, together with optical refocusing, are main issues for achieving fast and successful 3D RI reconstruction of weak objects. In particular, the optical refocusing is performed by a high-speed focus tunable lens mounted in front of the digital camera enabling compatibility with commercial microscopes. The technique is experimentally demonstrated on different examples: diatom cells (biosilica shells), polystyrene micro-spheres and blood cells. The results confirm the straightforward 3D-RI reconstruction of the samples providing valuable quantitative information for their analysis. Thus, the PC-ODT can be considered as an efficient and affordable alternative to coherent ODT which requires specially designed holographic microscopes.

OCIS codes: (100.3010) Image reconstruction techniques; (030.0030) Coherence and statistical optics; (120.4630) Optical inspection; (170.6900) Three-dimensional microscopy.

References and links

1. W. Choi, C. Fang-Yen, K. Badizadegan, S. Oh, N. Lue, R. Dasari, and M. Feld, "Tomographic phase microscopy," Nat. Meth. **4**, 717–720 (2007).
2. Y. Sung, W. Choi, C. Fang-Yen, K. Badizadegan, R. R. Dasari, and M. S. Feld, "Optical diffraction tomography for high resolution live cell imaging," Opt. Express **17**, 266–277 (2009).
3. Y. Cotte, F. Toy, P. Jourdain, N. Pavillon, D. Boss, P. Magistretti, P. Marquet, and C. Depeursinge, "Marker-free phase nanoscopy," Nat. Phot. **7**, 113–117 (2013).
4. T. Kim, R. Zhou, M. Mir, S. D. Babacan, P. S. Carney, L. L. Goddard, and G. Popescu, "White-light diffraction tomography of unlabelled live cells," Nat. Phot. **8** 256–263 (2014).
5. M. Born and E. Wolf, *Principles of Optics* (Cambridge University Press, Cambridge, 1999).
6. M. H. Jenkins and T. K. Gaylord, "Three-dimensional quantitative phase imaging via tomographic deconvolution phase microscopy," Appl. Opt. **54**, 9213 (2015).
7. M. Chen, L. Tian, and L. Waller, "3D differential phase contrast microscopy," Biomed. Opt. Express **9718**, 971826 (2016).
8. N. Streibl, "Three-dimensional imaging by a microscope," J. Opt. Soc. Am. A **2**, 121–127 (1985).
9. Y. Bao and T. K. Gaylord, "Quantitative phase imaging method based on an analytical nonparaxial partially coherent phase optical transfer function," J. Opt. Soc. Am. A **33**, 2125 (2016).
10. P. Ferraro, A. Wax, and Z. Zalevsky, *Coherent Light Microscopy: Imaging and Quantitative Phase Analysis*, Springer Series in Surface Sciences (Springer, 2011).
11. L. Turner, B. Dhal, J. Hayes, A. Mancuso, K. Nugent, D. Paterson, R. Scholten, C. Tran, and A. Peele, "X-ray phase imaging: Demonstration of extended conditions for homogeneous objects," Opt. Express **12**, 2960–2965 (2004).
12. D. S. C. Biggs, "3D deconvolution microscopy," Curr. Protoc. Cytom. 1–20 (2010).
13. D. Sage, L. Donati, F. Soulez, D. Fortun, G. Schmit, A. Seitz, R. Guiet, C. Vonesch, and M. Unser, "DeconvolutionLab2: An Open-Source Software for Deconvolution Microscopy," Methods **115**, 28–41 (2017).
14. J. A. Rodrigo and T. Alieva, "Rapid quantitative phase imaging for partially coherent light microscopy," Opt. Express **22**, 13472–83 (2014).
15. J. A. Rodrigo and T. Alieva, "Illumination coherence engineering and quantitative phase imaging," Opt. Lett. **39**, 5634–7 (2014).
16. S. Yamanaka, R. Yano, H. Usami, N. Hayashida, M. Ohguchi, H. Takeda, and K. Yoshino, "Optical properties of diatom silica frustule with special reference to blue light," J. Appl. Phys. **103**, 074701 (2008).

#295789 https://doi.org/10.1364/OE.25.015699
Journal © 2017 Received 11 May 2017; revised 15 Jun 2017; accepted 17 Jun 2017; published 26 Jun 2017

Optics EXPRESS

17. S. Spaulding, D. Lubinski, and M. Potapova, "Diatoms of the United States," "Available at: Westerndiatoms. colorado. edu, http://westerndiatoms.colorado.edu/taxa/species/cocconeis_placentula" (2010).
18. J. Lim, K. Lee, K. H. Jin, S. Shin, S. Lee, Y. Park, and J. C. Ye, "Comparative study of iterative reconstruction algorithms for missing cone problems in optical diffraction tomography," Opt. Express **23**, 16933–48 (2015).
19. J. Schindelin, I. Arganda-Carreras, E. Frise, V. Kaynig, M. Longair, T. Pietzsch, S. Preibisch, C. Rueden, S. Saalfeld, B. Schmid, J. Tinevez, D. J. White, V. Hartenstein, K. Eliceiri, P. Tomancak and A. Cardona, "Fiji: an open-source platform for biological-image analysis," Nat. Meth. **9**, 676–682 (2012).
20. J. Yoon, K. Kim, H. Park, C. Choi, S. Jang, and Y. Park, "Label-free characterization of white blood cells by measuring 3D refractive index maps," Biomed. Opt. Express **6**, 3865 (2015).
21. M. Diez-Silva, M. Dao, J. Han, C.-T. Lim, and S. Suresh, "Shape and biomechanical characteristics of human red blood cells in health and disease," MRS bulletin **35**, 382–388 (2010).
22. F. Charrière, A. Marian, F. Montfort, J. Kuehn, T. Colomb, E. Cuche, P. Marquet, and C. Depeursinge, "Cell refractive index tomography by digital holographic microscopy," Opt. Lett. **31**, 178–180 (2006).
23. B. Simon, M. Debailleul, M. Houkal, C. Ecoffet, J. Bailleul, J. Lambert, A. Spangenberg, H. Liu, O. Soppera, and O. Haeberlé, "Tomographic diffractive microscopy with isotropic resolution," Optica **4**, 460–463 (2017).
24. C. J. R. Sheppard, Y. Kawata, S. Kawata, and M. Gu, "Three-dimensional transfer functions for high-aperture systems," J. Opt. Soc. Am. A **11**, 593–598 (1994).

1. Introduction

The three-dimensional (3D) reconstruction of the cell structure and its refractive index (RI) are required for disease diagnosis as well as for estimation of the cell dry mass and volume, etc. Label-free microscopy is an attractive alternative to fluorescence imaging often applied for diverse cell studies. In the last decades different tomographic methods, such as computerized tomography or optical diffraction tomography (ODT) [1–4], have been realized in wide-field transmission microscopy by exploiting previous ideas proposed in 50th-70th of the last century [5]. Most of the successful, and now commercially available, ODT techniques (often called as tomographic phase microscopy) are based on digital holography and apply temporally and spatially coherent illumination sources (lasers). Instead of rotating the sample, in coherent ODT (C-ODT) the illumination beam is scanned by using for example a galvo-mounted mirror for coverage of the illumination angles [1, 2]. This is often referred to as beam rotation illumination and requires a temporal multiplexing approach to fill the maximum allowed 3D microscope aperture in order to reconstruct the 3D optical scattering potential, which is related to the refractive index of the sample. Thus, this technique involves the acquisition and the computational processing of significant volume of data. An alternative is using partially coherent illumination that can significantly reduce the data acquisition time (measuring a single stack of refocused intensity images), eliminate speckle noise and simplify the reconstruction process. Interestingly, for low spatial coherent illumination (fully opened condenser aperture) the bright-field microscope transmits the same object spatial-frequency content that the C-ODT is able to achieve from multiple illuminations. Thus, the partially coherent optical diffraction tomography (PC-ODT) seems a well-suited tool for 3D quantitative imaging and an alternative to the C-ODT. The benefits of partially coherent illumination, however, are accompanied by a lower image contrast that was probably one of the reasons why its potential has not been completely exploited yet. The quantitative phase imaging techniques reported in [6, 7] follow the seminal work of N. Streibl [8] devoted to 3D partially coherent imaging, where the expression of the phase and absorption optical transfer functions of the wide-field transmission microscope were derived assuming Born approximation in the paraxial limit. For example, in [6] the 3D reconstruction of the object RI is achieved by using tomography based on physical rotation of the object and deconvolution phase microscopy. While, in [7] a differential contrast (DIC) method for the 3D recovery of the real and imaginary part of the object RI has been proposed. Both methods are computationally demanding and require the recording of several stacks of refocused images.

The main goal of our work is to demonstrate that the 3D RI distribution of weak objects, such as cells and micro-organisms, can be easily reconstructed by using a PC-ODT technique developed for standard bright-field microscopes that exploits spatially low coherent illumination reaching

Optics EXPRESS

a spatial resolution similar to the one obtained by the C-ODT. A relevant advantage is that the proposed PC-ODT technique is fast in the RI reconstruction as well as in the measurement of the required stack of refocused intensity images. Specifically, the measurement setup consists of a programmable electrically tunable lens (ETL) incorporated after the tube lens of the microscope that allows for high-speed optical refocusing of the sample. Note that numerical refocusing cannot be applied for partially coherent illumination. Moreover, this technique assumes the non-paraxial regime and exploits the high numerical apertures of the objective NA_o and condenser NA_c providing the low spatially coherent illumination required for high transverse and axial resolution. We experimentally demonstrate that this is an optimal condition for achieving 3D quantitative imaging in a practical way. In the considered examples, the measurement was performed in 1.3 s with an exposure time of 10 ms while the computational reconstruction of the 3D RI of the object was typically achieved in a time of 8 s (using Matlab R2016a and Intel Xeon E5-1620v3 CPU). A rate of about 8 frames in 3D per second can be achieved by using an exposure time of 1 ms, which is compatible with further development of video-rate 3D imaging. To test the proposed PC-ODT technique, we have considered different objects such as diatoms, dielectric micro-particles and blood cells.

This work is organized as it follows. First, we describe the principle of the PC-ODT technique and compare it with the C-ODT. Then, in Section 3 the design of the proposed setup, data acquisition process and the deconvolution approach are discussed. Section 4 is devoted to the demonstration and discussion of the experimental results. The work ends with concluding remarks.

2. Principle of 3D imaging for coherent and partially coherent light

The goal of the ODT is the reconstruction of the optical scattering potential defined by the function $V(\vec{r}) = k_0^2(n^2(\vec{r}) - n_m^2)$, where: $\vec{r} = (x, y, z)$, $k_0 = 2\pi/\lambda_0$ with λ_0 being the free-space wavelength, while $n(\vec{r})$ and n_m are the refractive index of the specimen and its surrounding medium, correspondingly. The function $V(\vec{r})$ is real in the lossless case when the sample only modulates the phase of the transmitted field, thus $V(\vec{r}) = P(\vec{r})$, while it is a complex function $V(\vec{r}) = P(\vec{r}) + iA(\vec{r})$ if the sample absorption (given by $A(\vec{r})$) has to be taken into account.

It is well-known that the illumination of the specimen is important for achieving high-quality images but it also plays a crucial role in quantitative imaging techniques such as the ODT. In this work we consider the case of a bright-field transmission microscope (the light source can be a LED or a halogen lamp) where the specimen illumination is controlled by the aperture of the condenser lens. The opening and closing of the condenser aperture diaphragm (circular-like pupil) determines the ratio of spatial coherence, $S = NA_c/NA_o$, where NA_c and NA_o are the numerical apertures of the condenser and objective lens, correspondingly. Specifically, the coherent limit is reached at $S \to 0$ whereas $S \gg 2$ corresponds to the incoherent case [8]. Thus, as the condenser diaphragm is opened both NA_c and the effective numerical aperture of the microscope ($NA_c + NA_o$) reach their maximum values resulting in greater resolving power and light transmittance.

To study the role played by the illumination coherence ratio in the ODT, let us first recall the 3D imaging formation process for partially coherent light. By considering the first-order Born approximation, N. Streibl [8] derived that the 3D intensity image $I(\vec{r})$ in a bright-field microscope can be written as a linear superposition of the real and imaginary parts of the scattering potential convolved with the corresponding point spread functions (PSFs) $h_P(\vec{r})$ and $h_A(\vec{r})$ as it follows

$$I(\vec{r}) = B + P(\vec{r}) \otimes h_P(\vec{r}) + A(\vec{r}) \otimes h_A(\vec{r}), \tag{1}$$

with B being the background intensity (unscattered light). Here, $h_P(\vec{r})$ and $h_A(\vec{r})$ are the microscope response functions to a point scatter ($V(\vec{r}) = \delta(\vec{r})$) and to a point absorber ($V(\vec{r}) = i\delta(\vec{r})$), respectively. We recall that this expression can be applied for different illumination

Optics EXPRESS

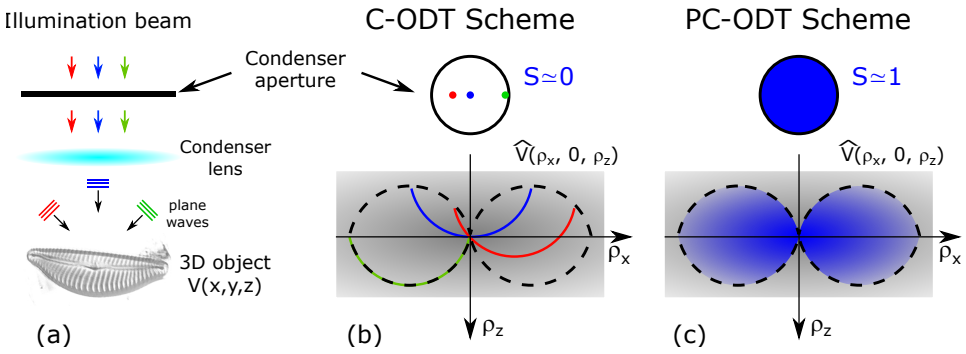

Fig. 1. (a) Illumination configuration for a transmission wide-field microscope. (b) The C-ODT technique retrieves the scattering potential spectrum $\widetilde{V}(\vec{\rho})$ transmitted by the microscope. An illumination scanning approach (sequential object illumination) is used to collect all the cross sections of the object's spectra with the Ewald sphere (semicircular arcs). As an example, only 3 scanning positions (thus 3 semicircular arcs) have been sketched. Note that the transmitted part of $\widetilde{V}(\vec{\rho})$ falls inside a 3D horn-torus in the reciprocal space, here only its section $(\rho_x, 0, \rho_z)$ has been sketched (dashed curve). (c) The proposed PC-ODT technique retrieves the same horn-torus region because the illumination of the condenser aperture allows for coverage of all the illumination angles simultaneously.

states by using a properly calculated or experimentally estimated functions $h_P(\vec{r})$ and $h_A(\vec{r})$. Nevertheless, in the C-ODT case a similar expression but for the complex field amplitude is often used [1, 3]. In this work, as in [8], we consider a circular-like condenser pupil and assume partially coherent illumination in the interval $S \in [0, 1]$.

The expression Eq. (1) has a straightforward interpretation in the reciprocal Fourier domain. Specifically, the 3D image spectrum −calculated as the 3D Fourier transform (FT) of the $I(\vec{r})$− is given by

$$\widehat{I}(\vec{\rho}) = B\delta(\vec{\rho}) + \widehat{P}(\vec{\rho})\, H_P(\vec{\rho}) + \widehat{A}(\vec{\rho})\, H_A(\vec{\rho}), \tag{2}$$

where $H_P(\vec{\rho})$ and $H_A(\vec{\rho})$ are the phase (POTF) and absorption (AOTF) optical transfer functions. Note that the POTF and the AOTF are the 3D-FT of $h_P(\vec{r})$ and $h_A(\vec{r})$, respectively. Indeed, the 3D image formation can be understood as a simple filtering process where the OTFs limit the observable object spectrum encoded as the 3D-FT of the scattering potential: $\widehat{V}(\vec{\rho}) = \widehat{P}(\vec{\rho}) + i\widehat{A}(\vec{\rho})$. The analytic expression for the POTF and AOTFs of a bright-field transmission microscope, with circular apertures (of both the condenser and the objective lens), have been derived for $S \in [0, 1]$ in the paraxial approximation by N. Strebil [8] and more recently by Y. Bao and T. Gaylord [9] for the non-paraxial case.

To illustrate the 3D imaging process and the differences between the C-ODT and the PC-ODT techniques, let us describe them following the sketch displayed in Fig. 1. We consider Köhler illumination configuration, where the optical field distribution in the condenser aperture serves as effective illumination source. In the case of C-ODT, a laser beam providing both temporally and spatially coherent illumination is focused onto the condenser aperture in order to obtain a plane wave illumination over the object. The direction of the plane wave depends on the position of the spot (focused laser beam) as it is indicated in Figs. 1(a) and 1(b). For each illumination angle of the plane wave (that depends on the spot position) only one cross section of the object spectrum $\widehat{V}(\vec{\rho})$ and the Ewald sphere can be retrieved. In general, an interferometric measurement (a hologram recorded by a digital camera) is often used to retrieve such a cross-section information. Specifically, the recovered information located within semicircular arcs, as the ones sketched in Fig. 1(b), is obtained via phase retrieval from the recorded hologram by using numerical refocusing and complex amplitude deconvolution. Thus the C-ODT, see for example [1, 3],

Optics EXPRESS

is achieved by scanning the laser beam throughout the entire condenser aperture that allows increasing the available frequency content till the limits (dashed curves) defined by NA_c and NA_o. In Fig. 1(b) such filling process used in C-ODT has been indicated only for 3 scanning positions (thus resulting in 3 semicircular arcs) to help the visualization. To construct the synthetic version of the object's $\widehat{V}(\vec{\rho})$ transmitted by the microscope, all the retrieved spectrum cross sections have to be assembled together in the reciprocal 3D space [1, 3]. This holographic time multiplexing process, which is characteristic of C-ODT, results computationally demanding and needs an interferometric setup with specialized hardware: e.g., fast galvanometer-controller mirrors to change the angle of incidence (beam rotation) and a high-speed camera recording the holograms.

In contrast to the C-ODT, the PC-ODT exploits quasi-monochromatic and spatially incoherent light provided by a LED or a halogen lamp to illuminate the entire condenser aperture, see Fig. 1(c). As a result, the object is simultaneously illuminated by the incoherent sum of plane waves emerging from different directions. Therefore, a similar part of the $\widehat{V}(\vec{\rho})$, see Fig. 1(c), transmitted by the microscope can be reconstructed from a single data set $I(\vec{r})$ obtained by optical refocusing (axial scanning). Thus, the PC-ODT is inherently faster than the C-ODT and, in practice, simplifies the measurement and the reconstruction process. An additional advantage is that the low spatial coherent illumination avoids coherent artifact noise such as speckle noise, which plagues C-ODT and other coherent light microscopy imaging methods [10]. Moreover, the partially coherent illumination enables compatibility with conventional commercial microscopes.

The ODT is often applied by assuming the pure phase specimen approximation ($V(\vec{r}) = P(\vec{r})$) that can simplify the deconvolution process. Nevertheless, as it was firstly pointed out by N. Strebil [8], one can apply the PC-OTD in the weak absorption regime by recording two or more data sets with different pupil functions, for example, a bright-field image and a phase-contrast image. Since the corresponding 3D OTFs are different, it should be possible determine both $A(\vec{r})$ and $P(\vec{r})$. Based upon this idea, it has been recently reported a 3D differential phase contrast microscopy technique [7] demonstrating recovery of $A(\vec{r})$ and $P(\vec{r})$ in the weak absorption regime. Such a technique requires four data sets, $I(\vec{r})$ stacks, one for each illumination configuration. Moreover, the reconstruction process used in [7] needs a computationally demanding method based upon the Total Variation (TV) deconvolution algorithm commonly used for deconvolution in fluorescence microscopy imaging.

An alternative approach, exploited here, is to assume that the absorption part of the scattering potential is proportional to the phase part ($A(\vec{r}) = \varepsilon P(\vec{r})$) under the weak absorption aproximation. This is often considered in a similar way for X-ray phase imaging [11]. In this approximation, a nearly phase 3D object can be easily recovered from

$$\hat{I}(\vec{\rho}) = B\delta(\vec{\rho}) + P(\vec{\rho}) \times \left[H_P(\vec{\rho}) + \varepsilon H_A(\vec{\rho})\right]. \tag{3}$$

by only using one intensity stack and the *effective* OTF: $H_E(\vec{\rho}) = H_P(\vec{\rho}) + \varepsilon H_A(\vec{\rho})$ where ε is a small $(0 - 0.1)$ empirically adjusted parameter. Note that $\varepsilon = 0$ corresponds to the case of pure phase specimens. In the considered examples we have used $\varepsilon = 0.05$, see Appendix for further details. The real part of the scattering potential $P(\vec{r})$ is calculated from its Fourier transform $P(\vec{\rho})$, which can be obtained by using the regularized Wiener deconvolution algorithm [12]:

$$P(\vec{\rho}) = \frac{\hat{I}(\vec{\rho})\, H_E^*(\vec{\rho})}{\left|H_E(\vec{\rho})\right|^2 + \beta}, \tag{4}$$

with previous background subtraction: $\hat{I}(\vec{\rho}) = I(\vec{\rho}) - B\delta(\vec{\rho})$. The typical values of the regularization parameter β defined by the signal to noise ratio (SNR) are $\beta \sim 10^{-2} - 10^{-4}$. The Eq. (4) provides direct and fast recovery of $P(\vec{\rho})$.

Optics EXPRESS

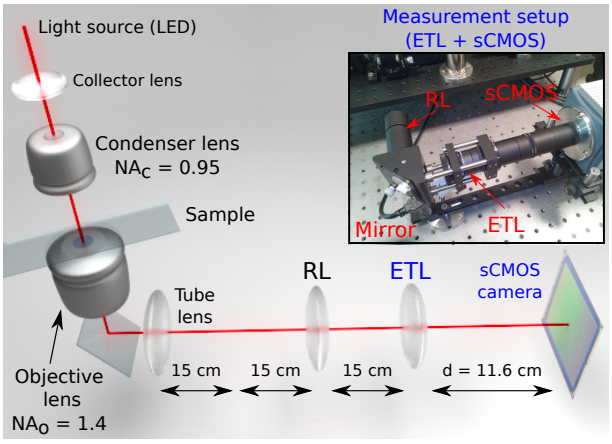

Fig. 2. Setup for the measurement of the stack of intensity images $I(\vec{r})$. The sample is imaged by the objective lens and tube lens. The obtained 3D image is then axially scanned by using the refocusing setup comprising the relay lens (RL) with focal length of 15 cm and the ETL lens with a varying focal length. The inset displays the measurement device: ETL (Optotune, EL-10-30-C) and a high-speed sCMOS camera (Hamamatsu, Orca Flash 4.0).

Finally, the real and imaginary parts of the refractive index, $n(\vec{r}) = n_{\mathrm{Re}}(\vec{r}) + \mathrm{i}n_{\mathrm{Im}}(\vec{r})$, are

$$n_{\mathrm{Re}}(\vec{r}) = \sqrt{\frac{\left|n^2(\vec{r})\right| + \mathrm{Re}\left\{n^2(\vec{r})\right\}}{2}}, \tag{5}$$

and

$$n_{\mathrm{Im}}(\vec{r}) = \sqrt{\frac{\left|n^2(\vec{r})\right| - \mathrm{Re}\left\{n^2(\vec{r})\right\}}{2}}, \tag{6}$$

with $n^2(\vec{r}) = P(\vec{r})k_0^{-2}(1 + \mathrm{i}\varepsilon) + n_m^2$. More sophisticated deconvolution algorithms could improve the recovery of $n(\vec{r})$, but they have to be specifically developed for the considered bright-field 3D imaging. Note that the available fluorescence deconvolution tools (either with direct or iterative approaches) [12, 13] cannot be applied because they are based on a priori constraints such as non-negativity of the PSF, which do not hold for both C-ODT and PC-ODT quantitative imaging.

In contrast to previously reported works devoted to partially coherent microscopy imaging, here we experimentally demonstrate that the 3D refractive index distribution of the specimen (similar to the one obtained by the C-ODT) can be straightforwardly reconstructed for the case of weakly absorbing samples by only measuring a single data set $I(\vec{r})$ in the microscope under low spatially coherent illumination ($S \sim 1$).

3. Implementation of the PC-ODT technique

In this work we propose a PC-ODT technique for quantitative 3D imaging by exploiting a high-NA of both objective lens (Olympus UPLSAPO, 100× $\mathrm{NA_o} = 1.4$, oil immersion, $n_{imm} = 1.518$) and Abbe condenser lens (Nikon, $\mathrm{NA_c} = 0.95$) that are available in commercial microscopes. A quasi-monochromatic illumination (central wavelength of $\lambda_0 = 450$ nm) is considered. The high NA of both lenses and low degree of light spatial coherence ($S \sim 0.7$) provide the optical sectioning capability required for 3D imaging as well as reasonably good trade-off between transverse $\Delta x = \Delta y = \lambda_0/(\mathrm{NA_o} + \mathrm{NA_c}) \approx 200$ nm and axial $\Delta z = \lambda_0/(n_{imm} - (n_{imm}^2 - \mathrm{NA_o^2})^{1/2}) \approx 500$ nm spatial resolution limits. The axial resolu-

Optics EXPRESS

tion limit does not depend on S, however, the optical sectioning depends on it because the entire volume of spatial frequencies transmitted through the system is governed by the coherence ratio.

The optical setup used for the automatic measurement of the stack of intensity images, $I(\vec{r})$, is easily attached to the microscope as sketched in Fig. 2. The sample is imaged by the objective lens and a tube lens, which is identical to the relay lens (RL) with a focal length of 15 cm. The measurement of $I(\vec{r})$ can be performed almost in real time by using optical refocusing (*axial scanning*) provided by a high-speed electrically tunable lens (ETL, Optotune, EL-10-30-C) located in the Fourier conjugated plane, thus avoiding image distortion arising from possible lens aberrations. Moreover, the applied telescopic configuration (RL and ETL) keeps a constant scaling of the recorded intensity images. The final magnification of the recorded images is $M = 64$ providing a good trade-off between the spatial resolution (mentioned above) and the field of view size, $52 \times 52\ \mu$m, required for a proper observation of the specimen. Note that the transverse resolution of the optical system almost coincides with the camera one. Specifically, the frequency cut-off of the camera (sCMOS, Hamamatsu, Orca Flash 4.0, 16-bit gray-level, pixel size $a = 6.5\ \mu$m) in the sample plane is $M \times a/2 = 4.9\ \mu\text{m}^{-1}$. The range of focal length of the ETL used in the experiments corresponds to a $z-$scanning interval of $\sim 10\mu$m with an axial step of $\Delta z_{scan} = 250$ nm in the sample domain. The ETL allows for fast measuring the intensity stack without any mechanical axial movement of the microscope's sample stage. Further information about the performance of this refocusing setup can be found in [14, 15]. In our case, as an example, a data set $I(\vec{r})$ comprising 130 images of 512×512 pixels has been measured in 1.3 seconds by using the high-speed sCMOS camera (exposure time of 10 ms). Nevertheless, the measurement can be performed with an exposure time of 1 ms providing a rate of about 8 frames in 3D per second, which is compatible with video-rate 3D imaging. Note that every intensity image of the stack has been normalized: $\sum_{i,j} I(i,j) = 1$, where i and j are the pixel indices.

For the case of high NA objective lens, $\text{NA}_\text{o} > 1$, the non-paraxial OTFs ($H_P(\vec{\rho})$ and $H_A(\vec{\rho})$) are required. In our case these OTFs have been calculated by adapting the expressions derived in [9], see Appendix. Here, we have also taken into account the low-pass filtering associated to the modulation transfer function ($\text{MTF}(\rho_x, \rho_y)$) of the camera by using $I(\vec{\rho}) \rightarrow I(\vec{\rho})\ /\text{MTF}(\rho_x, \rho_y)$ for every ρ_z. Then, the deconvolution algorithm described by Eq. (4) has been applied with a regularization parameter $\beta = 5 \times 10^{-4}$ according to the estimated SNR. Note that for the required background filtering the parameter B can be easily estimated by averaging the intensity of an empty region of the measured $I(\vec{r})$. In order to make faster the reconstruction process a region of interest of $373 \times 373 \times 64$ pixels in the stack $I(\vec{r})$ has been processed.

4. Experimental results and discussions

To test the feasibility of the proposed PC-ODT technique, here we consider different objects such as diatoms, polystyrene micro-spheres and blood cells whose shapes and RIs are well known. The diatoms are micro-organisms with transparent cell walls (known as frustule) made of silicon dioxide hydrated with a small amount of water. Such a biosilica frustule has a RI value $n_\text{Re} \sim 1.46$ [16] and typically consists of two halves called valves containing patterns of pores that allow nutrient and waste exchange with the environment since silica structure is impervious. The pores on the frustule may vary in the range of $0.1 - 1\ \mu$m, so they have a proper size and geometrical arrangement to test imaging techniques in microscopy including the ODT ones. Since the considered PC-ODT is designed for weak object approximation, the diatoms have to be immersed in a medium with a similar RI to fulfill this condition. Moreover, the diatoms have been cleaned with H_2O_2 to remove the highly absorbing algae they harbor inside preserving only the biosilica frustule. In our case, the diatoms have been immersed in oil (Olympus immersion oil type-F, $n_m = 1.518$) in order to achieve an appropriate RI contrast: $\Delta n = n_\text{Re} - n_m \approx -0.05$. Note that in this case $n_\text{Re} < n_m$ while in the other considered examples (e.g. micro-spheres and blood cells) a contrast $\Delta n > 0$ is considered for the completeness of the technique demonstration.

Optics EXPRESS

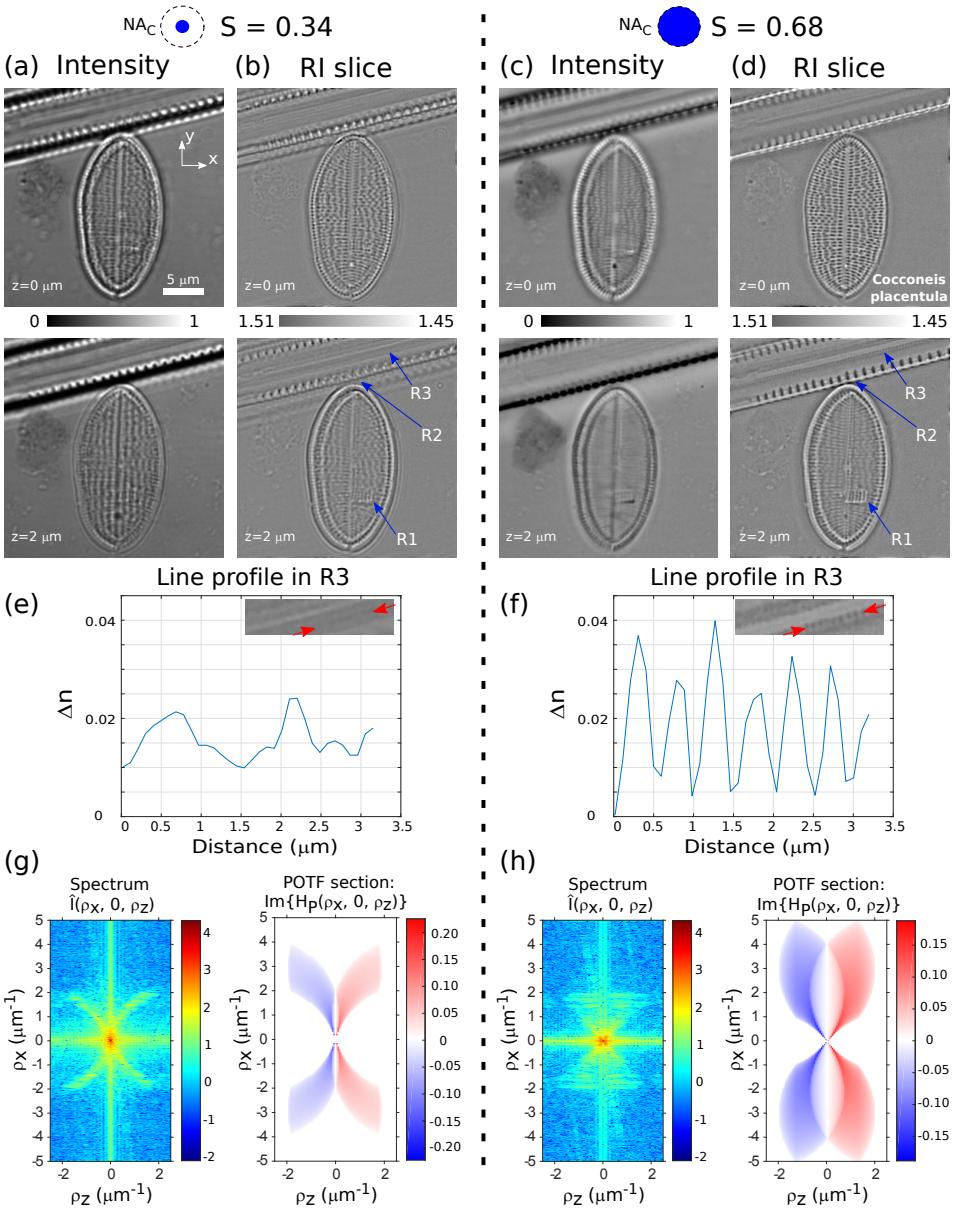

Fig. 3. Bright-field intensity images (slices extracted from the measured intensity stack $I(\vec{r})$) and the corresponding reconstruction of the refractive index (RI) for a *Cocconeis placentula* diatom obtained under two different illumination conditions: $S = 0.34$ for (a, b) and $S = 0.68$ for (c, d). The intensity and RI distributions (xy-slices) are displayed for two axial positions z in the first and second row. The measured intensity stack as well as the RI stack for both S values are provided in Visualization 1 and Visualization 2, respectively. (e) and (f) display a RI profile along region R3 for $S = 0.34$ and $S = 0.68$, correspondingly. (g) and (h) show a 2D section of the object intensity spectrum $\widehat{I}(\rho_x, 0, \rho_z)$ together with the POTF section $\mathrm{Im}\{H_P(\rho_x, 0, \rho_z)\}$ corresponding to the case $S = 0.34$ and $S = 0.68$.

The correct application of the proposed PC-ODT technique requires high $\mathrm{NA_c}$, $\mathrm{NA_o}$ and S (low degree of spatial coherence) at the same time. This allows exploiting the optical sectioning for proper 3D RI recovery from the measurement of only one stack $I(\vec{r})$ of bright-field intensity

Optics EXPRESS

images. Let us first illustrate this important fact by comparing the results obtained by using the same experimental setup with $NA_o = 1.4$ but different coherence states: $S = 0.34$ ($NA_c = 0.48$) and $S = 0.68$ ($NA_c = 0.95$). The measured stack of intensity images along with the reconstructed RI stack are provided for each case in Visualization 1 ($S = 0.34$) and Visualization 2 ($S = 0.68$). Figs. 3(a) and 3(d) display representative intensity images and RI slices extracted from such stacks, where a *Cocconeis placentula* diatom [17] is observed along with another rod-like diatom. In Figs. 3(a) and 3(b) the images present severe cross-talk between different layers of the diatoms due to the high spatial coherence achieved for $S = 0.34$. In contrast, for $S = 0.68$ the cross-talk effects are suppressed and the diatoms result well distinguished including their characteristic structural features such as the pores observed in the reconstructed RI slices of Fig. 3(d). This is explained by the increased optical sectioning achieved with $S = 0.68$ (low spatial coherence) that allows detecting tiny structures in both transverse and axial directions. For example, the detection of a small piece of another diatom wall (labeled as region R1) attached to *Cocconeis placentula* is much better observed for $S = 0.68$, see Fig. 3(d).

The low spatial coherence also permits well-resolved imaging of other structures such as the rectangular-shaped pores (size of $\sim 300-400$ nm long and ~ 450 nm wide) decorating the frustule of the *Cocconeis placentula,* see Fig. 3(d) at $z = 0$, that almost disappear at $z = 2\,\mu$m where relevant diatom structures such as its dorsal margins and raphe are observed. Moreover, for $S = 0.34$ the images of both diatoms result overlapped while for $S = 0.68$ they are correctly separated, see region R2 indicated in Figs. 3(b) and 3(d). From the reconstructed RI distribution it is also possible characterizing tiny diatom structures [see region R3 in Figs. 3(b) and 3(d)] that are hidden in the intensity images and non-resolvable for small values of S. Indeed, by comparing the RI line profile of the region R3 displayed in Figs. 3(e) and 3(f) one realizes that the smallest resolved pores (holes of 250 nm) can only be successfully detected for high S values. Let us underline that such periodic arrangement of nano-scale pores is imaged in a single $xy-$plane of the RI stack, thus illustrating the highly selective optical sectioning of the system achieved with low spatially coherent illumination. These results underline the important role played by the low spatial coherence in the imaging process and the RI reconstruction, which allows exploring the object in 3D providing useful quantitative information.

The optical sectioning can be also understood from the analysis of the 3D intensity spectra and the POTF corresponding to both coherence states, see the Figs. 3(g) and 3(h) where a slice of the spectra $\hat{I}(\rho_x, 0, \rho_z)$ and the imaginary part of the POTF $\mathrm{Im}\{H_P(\rho_x, 0, \rho_z)\}$ are displayed. Note that the intensity spectra seem to have an axial and transverse spatial frequency cut-off of $2\,\mu m^{-1}$. The axial frequency limit coincides with the frequency cut-off $\rho_z^{cut} = (n_{oil} - (n_{oil}^2 - \mathrm{NA}_o^2)^{1/2})/\lambda_0$ determined by the objective lens. While the transverse frequency limit observed in the spectra corresponds to the smallest structures of such diatoms, which is significantly lower than the corresponding frequency cut-off of the optical system. It is well-known from scanning electron microscope images of diatoms that they are typically decorated with structures [17] in the scale of $0.1 - 1\,\mu$m (in Fig. 3(d) the pores of about $0.25 - 0.8\,\mu$m are distinguished) as well as with nano-scale structures $5 - 10$ nm beyond the optical resolution limit. Thus, the observed spatial frequency limits are in good agreement with the expected ones for diatoms. Note that for a low value of S the intensity spectrum has the shape of two thin semicircular arcs that fit in with the form of the corresponding POTF, see left panel of Fig. 3(g). Only the frequency content that lies within non-zero POTF region is transmitted by the bright-field microscope. In the case of low spatial coherence [$S = 0.68$, see Fig. 3(h)] there is a significantly improved lateral resolution limit $\rho_x^{cut} = 5\,\mu\mathrm{m}^{-1}$ compared with $\rho_x^{cut} = 3.9\,\mu\mathrm{m}^{-1}$ reached for $S = 0.34$. Moreover, the axial cone of missing frequencies in the POTF is significantly smaller for $S = 0.68$. We recall that the well-known missing cone effect (see for example [18]) is responsible for an artificial object elongation along the optical axis and for the cross-talk issues in the image and RI reconstruction. Such cross-talk issues are more severe for higher spatial coherence and for larger object size,

Optics EXPRESS

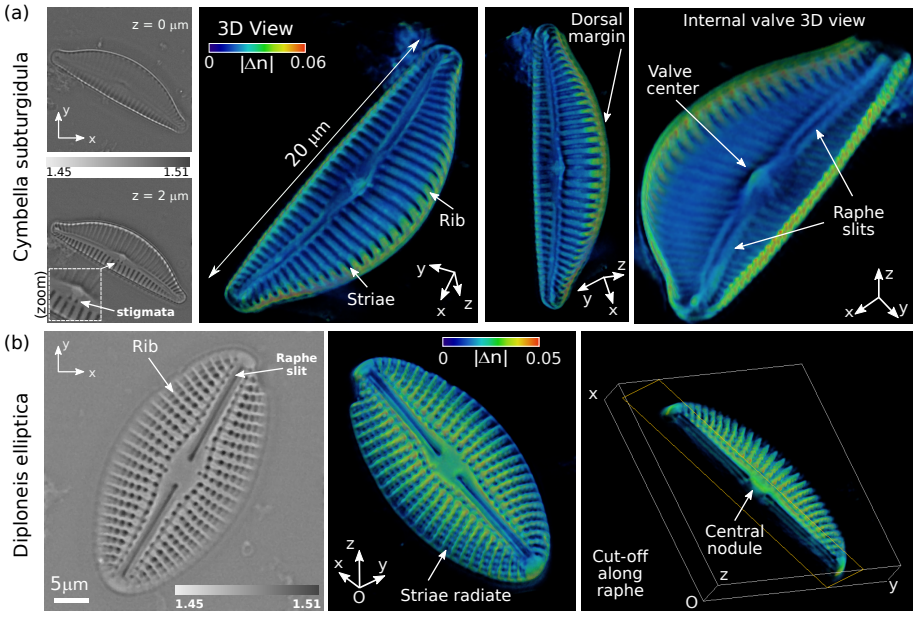

Fig. 4. (a) Reconstructed RI for a *Cymbella subturgidula* diatom. The frustule made of biosilica exhibits distinct structures such as slits and striae comprising the valves. Two $xy-$RI slices are presented in the first column where two tiny *stigmata* are observed close to the valve center, at $z = 2\ \mu$m. The following three columns are different points of view for 3D-RI ($|\Delta n| = |n_{\mathrm{Re}} - n_m|$) where different structures of the diatom are observed. (b) Reconstructed RI for a *Diploneis elliptica* diatom. In the first column, the $xy-$ RI slice reveals detailed structures such as the *raphe* slits and the pores comprising the diatom striae. The next two columns include different perspectives of the 3D-RI $|\Delta n|$, in which it is observed a rounded central area (*nodule*) located in the middle of a longitudinal canal (*raphe*). A 3D animated version of these diatoms (RI volume) is provided in Visualization 4 and Visualization 5, correspondingly.

thus underlying the need of using a low spatially coherent illumination ($S \sim 1$) to obtain reliable quantitative imaging. As observed in the POTF sections displayed in Figs. 3(g) and 3(h), the $\mathrm{Im}\{H_P\}$ is a function that has opposite sign for positive and negative frequencies in the axial direction ρ_z.

To test the performance of the proposed PC-ODT technique, we have also considered a sample comprising polystyrene spheres (bead diameter of 3.73 μm, $n_{\mathrm{Re}} = 1.6$, Spherotech Lot. AD01) immersed in oil ($n_m = 1.56$, Cargille Labs Series A) as a surrounding medium, see Appendix. The RI value of the polystyrene bead has been properly determined ($n_{\mathrm{Re}} = 1.59 \pm 0.01$) as well as the reconstructed shape of the sphere in the middle plane. However, the reconstructed bead suffers from some elongation along the axial direction due to the missing-cone issue. This well-known axial distortion effect is also present in C-ODT as well as in other quantitative imaging techniques, see for example [7, 18] where dielectric spheres of similar size have been studied. Such missing-cone issue is more severe for higher spatial coherence.

As it has been demonstrated, the proposed PC-ODT technique provides an optical sectioning capability well suited for 3D quantitative imaging. To further illustrate this fact, Fig. 4 displays the RI rendered as a 3D volume [19] corresponding to two different diatoms: *Cymbella subturgidula* [Fig. 4(a)] and *Diploneis elliptica* [Fig. 4(b)] specimens. The *Cymbella subturgidula* diatom has dorsi-ventral valves and exhibits bluntly rounded and barely protracted apices. Moreover, the dorsal margin of this diatom is strongly arched whereas the middle striae is slightly convex as

Optics EXPRESS

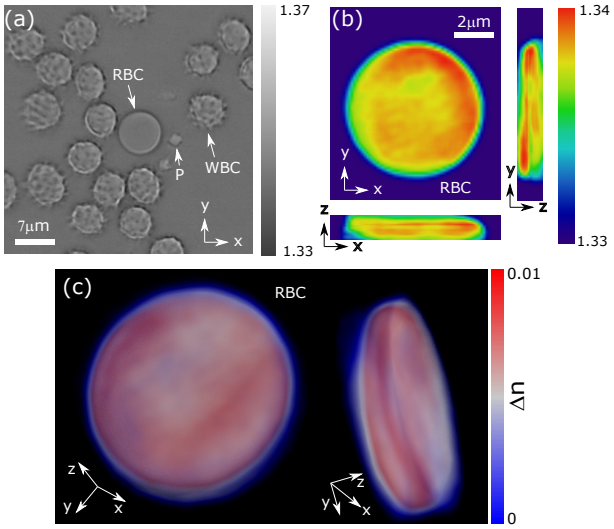

Fig. 5. (a) Refractive index slice of a blood smear where red blood cell (RBC), white blood cells (WBC) and platelets (P) are observed. (b) Close-up view of the refractive index slice of the RBC along $xy-$, $yz-$, and $xz-$planes. (c) 3D refractive index distribution (Δn) of the RBC exhibiting its characteristic biconcave disc-like shape.

displayed in Fig. 4(a). The curvature of the radiate striae (finely punctate) as well as tiny features such as isolated stigmata ($\sim$ 350 nm diameter, see zoom inset) have been also successfully reconstructed. This 3D structural information is particularly useful for the specimen classification and for the study of other biological characteristics. The size of the *Cymbella subturgidula* is about 20 μm long and 8 μm wide, which is in good agreement with the typical dimensions measured by using a scanning electron microscope (SEM) [17]. Figure 4(b) shows a symmetrical *Diploneis elliptica* diatom of 32.5 μm long and 17.3 μm wide exhibiting a density of 8 resolvable radiate striae along 10μm, that is also in good agreement with SEM data [17]. Indeed, the striae are radiate mid-valve, becoming arched towards the valve apices. Furthermore, the terminal *raphe* fissures deflect near of the valve margin [see the diatom apices in Fig. 4(b)]. The stack of intensity images alongside the corresponding RI slices are given in Visualization 3. Moreover, a 3D animated version of these diatoms (RI volume) is provided in Visualization 4 and Visualization 5, correspondingly.

The RI values (n_{Re} in the range $1.45 - 1.47$) obtained for the biosilica wall of the diatoms are consistent with those reported in the literature [16]. Nevertheless, these values vary depending on the diatom region: $n_{\mathrm{Re}} \sim 1.51$ in the striae, $n_{\mathrm{Re}} \sim 1.46 - 1.48$ in the ribs and $n_{\mathrm{Re}} \sim 1.45 - 1.46$ in the dorsal margin. This fact can be explained by the diversity of perforations present in the diatom structure. Indeed, the immersion oil fills the larger pores (in the striae) and thus yields an artificial increase of the RI comparing with the non-porous zones. Consequently, the more reliable values of the frustule RI are found in the more homogeneous biosilica regions such as the dorsal margin for the *Cymbella subturgidula* specimen [corresponding to $|\Delta n| = 0.05$ and $n_{\mathrm{Re}} = 1.46$, see Fig. 4(a)] or the central nodule of the *Diploneis elliptica* [corresponding to $|\Delta n| = 0.04$ and $n_{\mathrm{Re}} = 1.47$, Fig. 4(b)].

Finally, we study the performance of the PC-ODT technique for free-label analysis of living cells. In particular, we have analyzed a human blood sample just immediately after its extraction. The RI slice displayed in Fig. 5(a) shows red blood cells (RBCs), white blood cells (WBCs) and platelets (P) immersed in the blood plasma. Note that in this case $\Delta n > 0$. The reconstructed RI (n_{Re}) values are $n_{\mathrm{RBC}} = 1.34$ for the RBC and $n_{\mathrm{WBC}} = 1.36$ for the WBC. These results are in

Optics EXPRESS

good agreement with those obtained by other techniques including C-ODT [20]. The RI slices displayed in Fig. 5(b) and the 3D RI reconstruction shown in Fig. 5(c) demonstrate the typical biconcave disc shape of a healthy human RBC.

These promising results pave the way to the PC-ODT application in biomedicine. We recall that the 3D RI recovery is particularly interesting as a diagnosis tool. For instance, it can be used to track abnormalities in the shape of the RBCs or changes in their chemical properties [18] allowing illnesses detection [21]. The proposed technique is useful to reconstruct relevant structural features of the diatoms required for the analysis and classification of such micro-organisms, which is important for example to gather information about the environment where they live [17].

5. Conclusions

We have demonstrated that 3D quantitative imaging of weak scattering and absorption objects is possible by using a standard bright-field transmission microscope thanks to a straightforward PC-ODT technique. The measurement is performed by an electrically tunable lens and a sCMOS camera that allow for fast programmable and automatic acquisition of a single stack of bright-field intensity images, which is required for 3D reconstruction of the object refractive index. It has been proven that the high NA of the condenser and objective lens, as well as the low spatial coherence of the illumination, provide the required spatial resolution and optical sectioning crucial for 3D quantitative imaging. The dynamic range of the digital camera along with its MTF and the SNR have also been taken into account. The development of more sophisticated deconvolution algorithms especially designed for PC-ODT will further improve the RI reconstruction. If needed, the persisting missing-cone issue can be mitigated by including object rotation [22, 23]. We envision that the PC-ODT can be an alternative to the C-ODT.

Appendix

Analytical expression for the non-paraxial OTF.

According to [9] the phase and absorption parts of the non-paraxial OTF are given by

$$H_P(\rho_\perp, \rho_z) = \frac{\mathrm{i}\lambda}{4\pi}\left[F(\rho_\perp, \rho_z) - F(\rho_\perp, -\rho_z)\right], \tag{7}$$

$$H_A(\rho_\perp, \rho_z) = \frac{\lambda}{4\pi}\left[F(\rho_\perp, \rho_z) + F(\rho_\perp, -\rho_z)\right], \tag{8}$$

where $\lambda = \lambda_0/n_{imm}$ is the normalized wavelength (n_{imm} refers to the RI of the immersion oil of the objective lens) and

$$F(\rho_\perp, \rho_z) = \frac{\rho_\perp^2 \sigma}{\rho^2 \rho_z}\sqrt{\lambda^{-2} - \frac{\rho^2}{4} - \frac{\rho^2\sigma^2}{\rho_z^2}} + \left(\sqrt{\lambda^{-2} - \frac{\rho^2}{4}} - \frac{\rho_z^2}{2\rho}\right)\arccos\left(\frac{\rho\sigma}{\rho_z\sqrt{\lambda^{-2} - \rho^2/4}}\right). \tag{9}$$

The parameter σ has different values depending on the frequency region. When $0 < \rho_\perp < \rho_P - \rho_S$ it is given by:

$$\sigma = \begin{cases} \frac{\rho_z}{\rho_\perp}\left(\frac{\rho_z}{2} - \sqrt{\lambda^{-2} - \rho_S^2}\right) \\ \text{If}\left[\sqrt{\lambda^{-2} - \rho_S^2} - \sqrt{\lambda^{-2} - (\rho_S - \rho_\perp)^2} \le \rho_z \le \sqrt{\lambda^{-2} - \rho_S^2} - \sqrt{\lambda^{-2} - (\rho_S + \rho_\perp)^2}\right] \end{cases}, \tag{10}$$

while for $\rho_P - \rho_S < \rho_\perp < \rho_P + \rho_S$

Optics EXPRESS

$$\sigma = \begin{cases} \frac{\rho_z}{\rho_\perp}\left(\frac{\rho_z}{2} - \sqrt{\lambda^{-2} - \rho_S^2}\right) \\ \text{If } \left[\sqrt{\lambda^{-2} - \rho_S^2} - \sqrt{\lambda^{-2} - (\rho_S - \rho_\perp)^2} \le \rho_z \le \sqrt{\lambda^{-2} - \rho_S^2} - \sqrt{\lambda^{-2} - \rho_P^2}\right] \\ \frac{\rho_z}{\rho_\perp}\left(-\frac{\rho_z}{2} - \sqrt{\lambda^{-2} - \rho_P^2}\right) \\ \text{If } \left[\sqrt{\lambda^{-2} - \rho_S^2} - \sqrt{\lambda^{-2} - \rho_P^2} \le \rho_z \le \sqrt{\lambda^{-2} - (\rho_P - \rho_\perp)^2} - \sqrt{\lambda^{-2} - \rho_P^2}\right] \end{cases}, \quad (11)$$

where $\rho_\perp = \sqrt{\rho_x^2 + \rho_y^2}$ denotes the radial transverse frequency and ρ_z is the axial frequency, while $\rho_S = \mathrm{NA_c}/\lambda_0$ and $\rho_P = \mathrm{NA_o}/\lambda_0$. Note that the coherence ratio can be rewritten as $S = \rho_S/\rho_P$.

RI reconstruction with the effective OTF and the POTF

The advantage of the introduction of the effective OTF function is demonstrated in Fig. 6 where a $xy-$slice of n_{Re} reconstructed by using the effective OTF [see Fig. 6(a)] and only the POTF [see Fig. 6(b)] are displayed. It is observed that the consideration of weak absorption allows significantly reducing the halo artifacts related to low spatial frequencies gathered near the axis $\rho_z = 0$. We underline that these frequencies are mostly transmitted due to the AOTF. The assumption of the weak absorption approximation provides a more reliable reconstruction of the object structure.

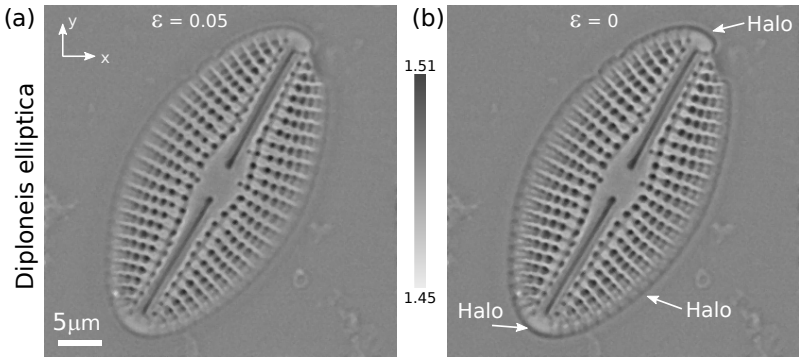

Fig. 6. (a) $xy-$slice of the RI reconstructed by using the effective OTF, $H_E(\vec{\rho}) = H_P(\vec{\rho}) + \varepsilon H_A(\vec{\rho})$, with $\varepsilon = 0.05$. (b) The reconstructed RI exhibits halo artifacts when only the POTF ($\varepsilon = 0$) is used.

Testing the PC-ODT technique

Here, we consider polystyrene spheres ($n_{\mathrm{Re}} = 1.6$ at $\lambda_0 = 450$ nm) immersed in oil ($n_m = 1.56$) in order to test the performance of the proposed PC-ODT technique. Figure 7 displays transverse and axial slices of the measured intensity and reconstructed RI distributions. The diameter of the sphere 3.8 ± 0.1 μm is close to the expected value of 3.7 μm. The RI value in the central region of the bead is $n_{\mathrm{Re}} = 1.59 \pm 0.01$ that is in good agreement with the expected one as well. As a consequence of the *missing-cone* issue ([7, 18, 24]), which is associated with a lack of low axial frequencies transmitted by the microscope, the reconstructed sphere suffers from an elongation along the $z-$axis. The halo observed around the sphere is also attributed to this problem. These effects has been observed in other studies as well [7, 18].

Optics EXPRESS

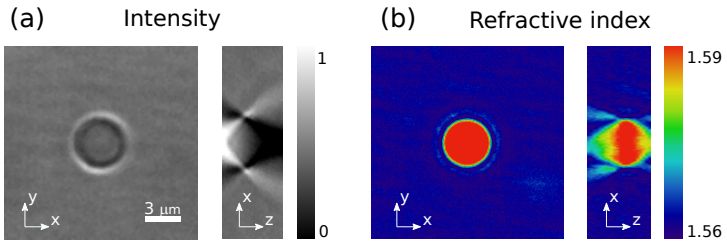

Fig. 7. (a) $xy-$slice of the bright-field intensity for a polystyrene sphere (bead diameter of $3.8 \pm 0.1\ \mu$m, $n_{\mathrm{Re}} = 1.59 \pm 0.01$, Spherotech Lot. AD01) immersed in oil ($n_m = 1.56$, Cargille Labs Series A). (b) Reconstructed refractive index for the same $xy-$slice.

Funding

Ministerio de Economía y Competitividad (TEC2014-57394-P).